PNAS RESEARCH ARTICLE | CHEMISTRY

Boosted C–C coupling with Cu–Ag alloy sub-nanoclusters for CO_2-to-C_2H_4 photosynthesis

Yangyang Yu[a,b], Ye He[c], Ping Yan[a], Shengyao Wang[d], and Fan Dong[a,b,1]

Edited by Alexis Bell, University of California, Berkeley, CA; received May 2, 2023; accepted September 7, 2023

The selective photocatalytic conversion of CO_2 and H_2O to high value-added C_2H_4 remains a great challenge, mainly attributed to the difficulties in C–C coupling of reaction intermediates and desorption of C_2H_4* intermediates from the catalyst surface. These two key issues can be simultaneously overcome by alloying Ag with Cu which gives enhanced activity to both reactions. Herein, we developed a facile stepwise photodeposition strategy to load Cu–Ag alloy sub-nanoclusters (ASNCs) on TiO_2 for CO_2 photoreduction to produce C_2H_4. The optimized catalyst exhibits a record-high C_2H_4 formation rate (1110.6 ± 82.5 μmol g^{-1} h^{-1}) with selectivity of 49.1 ± 1.9%, which is an order-of-magnitude enhancement relative to current work for C_2H_4 photosynthesis. The in situ FT-IR spectra combined with DFT calculations reveal the synergistic effect of Cu and Ag in Cu–Ag ASNCs, which enable an excellent C–C coupling capability like Ag and promoted C_2H_4* desorption property like Cu, thus advancing the selective and efficient production of C_2H_4. The present work provides a deeper understanding on cluster chemistry and C–C coupling mechanism for CO_2 reduction on ASNCs and develops a feasible strategy for photoreduction CO_2 to C_2 fuels or industrial feedstocks.

photocatalytic CO_2 reduction | C_2H_4 | Cu–Ag alloy sub-nanoclusters | C–C coupling | C_2H_4* desorption

Photocatalytic conversion of carbon dioxide (CO_2) and water (H_2O) to fuels or industrial feedstocks has raised significant broad interest considering that it can utilize solar energy as the driving force to reduce greenhouse gases and alleviate energy/resource shortages (1, 2). The current products in CO_2 photoreduction systems are mainly limited to C_1 fuels such as carbon monoxide (CO) and methane (CH_4) (3–6). However, high value-added industrial feedstocks have rarely been achieved from CO_2 photoreduction. Ethylene (C_2H_4) is the largest feedstock in petrochemical industries, and its production scale marks the national development level (7, 8). Therefore, among all the possible CO_2 reduction products, C_2H_4 has been regarded as the most promising one.

In recent years, researchers have devoted themselves to photocatalytic conversion of CO_2 and H_2O to C_2H_4 (9, 10). These results confirm the feasibility of photocatalytic reduction of CO_2 to C_2H_4, but even with the introduction of heat, sacrificial agents, or cocatalysts in these studies, the yield of C_2H_4 is still low (26.6 μmol $g^{-1}h^{-1}$). This is because of the difficulty for these catalysts to both promote C–C coupling of intermediates and to induce desorption of C_2H_4* from their surfaces. Cu metal has been considered one of the most attractive cocatalysts for CO_2 photoreduction as a result of its optimal binding energy with reaction intermediates, which could facilitate the reduction of CO_2 to a wide variety of hydrocarbons (11). In the electrochemical reduction of CO_2, Cu-based catalysts have been recognized as the only catalyst capable of producing the C_2H_4 (12–15). However, the utilization of Cu as a catalyst or cocatalyst in photoreduction of CO_2 rarely exhibits a similar ability to form C_2H_4 as that in electrochemical CO_2 reduction (16–21). This difference may be due to the poor stability of Cu in the photocatalytic process (22) or the different driving forces for the CO_2 reduction reaction between photocatalysis and electrocatalysis (23).

It is difficult for a single metal cocatalyst to possess both excellent C–C coupling performance and strong desorption ability of C_2H_4* intermediates. However, the construction of bimetallic co-catalysts if properly designed could enable the catalysts with these capabilities. Recently, some work has explored the binary combinations of Cu and noble metal cocatalysts in CO_2 photoreduction (24–26). However, these explorations are not dedicated to both promotion of C–C coupling and desorption of C_2H_4* from the catalytic surface, so that no C_2H_4 product are obtained, although they obtained high yield of CO or CH_4. However, we speculate that Cu–Ag alloy can effectively promote the C–C coupling of intermediates and obtain a high C_2H_4 yield. This is because the work function of Ag (4.26 eV) is lower than that of Cu (4.65 eV) (27), which can facilitate the transfer of hot electrons on Ag to Cu. In addition, the strong interfacial dielectric coupling between the Ag

Significance

Photocatalytic conversion of CO_2 and H_2O to C_2H_4 has raised significant broad interest considering that it can utilize solar energy as the driving force to obtain high value-added C_2H_4 and reduce greenhouse gases. This research prepared Cu–Ag alloy sub-nanoclusters (ASNCs) and obtained a record-high C_2H_4 formation rate. This study reveals the synergistic effect of Cu and Ag in Cu–Ag ASNCs, which enable an excellent C–C coupling capability like Ag and promoted C_2H_4* desorption property like Cu, thus advancing the selective and efficient production of C_2H_4. The present work provides a deeper understanding on C–C coupling mechanism and develops a feasible strategy for photoreduction CO_2 to C_2product.

Author affiliations: [a]Research Center for Carbon-Neutral Environmental & Energy Technology, Institute of Fundamental and Frontier Sciences, University of Electronic Science and Technology of China, Chengdu 611731, China; [b]Yangtze Delta Region Institute (Huzhou), University of Electronic Science and Technology of China, Huzhou 313000, China; [c]School of Resources and Environment, University of Electronic Science and Technology of China, Chengdu 611731, China; and [d]College of Science, Huazhong Agricultural University, Wuhan 430070, China

Author contributions: F.D. designed research; Y.Y. performed research; P.Y., S.W., and F.D. contributed new reagents/analytic tools; Y.Y., Y.H., and F.D. analyzed data; and Y.Y. wrote the paper.

The authors declare no competing interest.

This article is a PNAS Direct Submission.

[1]To whom correspondence may be addressed. Email: dfctbu@126.com or dongfan@uestc.edu.cn.

This article contains supporting information online at https://www.pnas.org/lookup/suppl/doi:10.1073/pnas.2307320120/-/DCSupplemental.

Published October 23, 2023.

plasma metal nanoclusters (<2 nm) and TiO_2 enables the formation of an interface state (IFS), resulting in the direct generation of hot electrons in TiO_2 under visible light, which would migrate to the surface of Ag and substantially enhance the CO_2 photoreduction activity of the catalyst (28, 29). More importantly, it has been reported that Ag/TiO_2 can effectively convert CH_4 to C_2H_4, indicating that Ag metal can effectively promote the C–C coupling reaction from CH_2* (30).

It is generally believed that the photocatalytic activity of the catalyst is closely related to the size of the metal cocatalysts (31). Metal sub-nanoclusters (<1 nm) can not only achieve sufficient exposure of atoms like single atoms but also have high stability. Their electronic properties are very different from those of metal nanoclusters (1–2 nm) and metal nanoparticles (2–100 nm). So their interaction with reactants is different from that of nanoclusters and nanoparticles, and these properties enable metal sub-nanoclusters with exceptionally excellent catalytic performance (32). Therefore, it is a feasible and innovative strategy to load the Cu–Ag alloy sub-nanoclusters (ASNCs) on the photocatalyst to enhance its CO_2 reduction performance.

In this work, we developed a facile stepwise photodeposition strategy to load Cu–Ag ASNCs on the flow sites of photogenerated electrons of TiO_2 (denoted as Cu_xAg_{1-x}/TiO_2, where x = 0, 0.2, 0.4, 0.6, 0.8, and 1.0 corresponding to at % Cu) for the photocatalytic conversion of CO_2 and H_2O to C_2H_4. The alloying Ag for C–C coupling with Cu for C_2H_4* desorption will give enhanced activity to both reactions. Among the Cu_xAg_{1-x}/TiO_2 series, $Cu_{0.8}Ag_{0.2}/TiO_2$ demonstrates the highest CO_2 photoreduction performance, and the formation rates for C_2H_4 and CH_4 are 1110.6 ± 82.5 and 1628.5 ± 108.3 μmol g^{-1} h^{-1}, respectively. The C_2H_4 formation rate (1110.6 ± μmol g^{-1} h^{-1}) with selectivity of 49.1 ± 1.9% is record-high with an order-of-magnitude enhancement relative to current work on photocatalytic conversion of CO_2 and H_2O (*SI Appendix,* Table S2). This is because the synergistic effect of Cu and Ag not only endows the Cu–Ag ASNCs with excellent C–C coupling capability like Ag, but also with excellent C_2H_4* desorption properties like Cu, thus promoting the selective production of C_2H_4. This work reveals the role of the synergistic effect of Cu and Ag in the Cu–Ag ASNCs in the activation of CO_2, C–C coupling of CH_2* intermediates, and C_2H_4* desorption from the catalyst, leading to highly boosted photocatalytic conversion of CO_2 and H_2O to C_2 fuels or industrial feedstocks.

Results

Surface Characterization of Catalysts. The composition, structure, and distribution of Cu–Ag ASNCs on TiO_2 were investigated by HAADF and HAADF-STEM. As shown in *SI Appendix,* Fig. S1, TiO_2 morphology is nanoparticles with diameters of 25–50 nm. The HAADF images reveal that Ag nanoparticles with inhomogeneous particle size (~ 5 nm) are distributed on the surface of TiO_2 in Ag/TiO_2, while the size of the Cu–Ag alloy on the surface of TiO_2 gradually decreases with the increase of Cu content, and for $Cu_{0.8}Ag_{0.2}/TiO_2$ and Cu/TiO_2, only metal sub-nanoclusters can be found distributed on the surface of TiO_2 (*SI Appendix,* Figs. S2 and S3). This is because the reduction potential of Ag (Ag^+/Ag, E^0 = +0.80 V) (33) is much higher than that of Cu (Cu^{2+}/Cu, E^0 = +0.34 V) (34, 35), which results in a much faster growth rate of Ag than Cu in the photodeposition process. HAADF-STEM images show that the metal sub-nanoclusters in the $Cu_{0.8}Ag_{0.2}/TiO_2$ are anchored evenly over the surface of TiO_2, and the sizes of metal sub-nanoclusters are rather small with a narrow size distribution of 0.71 ± 0.16 nm (Fig. 1 *A* and *C* and *SI Appendix,* Figs. S3 *A*–*C*). As shown in Figs. 1 *A* and *B* and *SI Appendix,* Figs. S3 *D* and *E*, the metal sub-nanoclusters display the characteristic spacing of 0.225 nm, which is between the lattice spacing of {111} lattice planes of Cu (0.209 nm, JCPDS 04-0836) and Ag (0.236 nm, JCPDS 04-0783), proving that the metal sub-nanoclusters are Cu–Ag alloys. In addition, the STEM mapping (circled part in Fig. 1*E*) further confirms that the Cu–Ag alloy sub-nanoclusters are formed on TiO_2 and that the Cu–Ag alloys contain more Cu than Ag (Fig. 1 *D*–*G*).

The content of Cu and Ag in the catalyst was detected by ICP-OES characterization. As shown in *SI Appendix,* Table S1, the molar content of Cu in $Cu_{0.8}Ag_{0.2}/TiO_2$ was about 0.6%, which is lower than the amount of Cu^+ (0.8 %) added during catalyst preparation, indicating that there is a loss of Cu in the catalyst preparation process. The crystal phase of catalysts was further confirmed by XRD. As shown in *SI Appendix,* Fig. S5*A*, only diffraction peaks associated with TiO_2 are found (JCPDS 38-0741 and JCPDS 21-1276), because the contents of Cu and Ag were below the lower detection limit of XRD (*SI Appendix,* Table S1). The XPS was further carried out to characterize the surface states of catalysts, and the results are shown in Fig. 2. The Ag $3d_{5/2}$ and Ag $3d_{3/2}$ peaks are observed at 367.7 and 373.7 eV respectively, which can be assigned to Ag^0 (Fig. 2*A*) (36). The Cu 2p orbitals presented at 932.6 and 952.3 eV belong to Cu $2p_{3/2}$ and Cu $2p_{1/2}$ of Cu^+ and/or Cu^0 species, respectively (Fig. 2*B*) (37). Since the XPS spectra make it difficult to distinguish Cu^+ from Cu^0, the Cu LMM XAES was applied to distinguish the different chemical states. As shown in *SI Appendix,* Fig. S4, the two overlapped peaks at 564.9 eV and 567.9 eV were ascribed to the kinetic energy of Cu^0 and Cu^+, respectively (38). In Cu/TiO_2 and $Cu_{0.8}Ag_{0.2}/TiO_2$, the content of Cu^0 is much higher than that of Cu^+, indicating that in Cu/TiO_2 and $Cu_{0.8}Ag_{0.2}/TiO_2$, Cu is mainly in the form of Cu^0. In addition, the content of Cu^+ in $Cu_{0.8}Ag_{0.2}/TiO_2$ is much lower than that of Cu in Cu/TiO_2, indicating that Ag increases the stability of Cu^0 in the Cu–Ag alloys. The binding energies (BEs) of Ag $3d_{5/2}$ and Ag $3d_{3/2}$ are positively shifted to 370.0 and 374.0 eV in the $Cu_{0.8}Ag_{0.2}/TiO_2$ (Fig. 2*A*), while the BEs of Cu $2p_{3/2}$ and Cu $2p_{1/2}$ shift negatively to 931.8 and 951.5 eV which are assigned to Cu^0 (Fig. 2*B*) (24). This result indicates the electron transfer from Ag to Cu in Cu–Ag alloy nanoclusters, which enhances the stability of Cu^0. Moreover, the presence of a portion of Cu^+ in Cu sub-nanoclusters also implies that the electrons are transferred from Ag to Cu (39). As shown in Fig. 2*C*, compared to TiO_2, the Ti 2p peaks of Ag/TiO_2 remain unchanged, while the Ti2p peak of Cu/TiO_2 and $Cu_{0.8}Ag_{0.2}/TiO_2$ has a significant negative shift. This is because the small contact interface between large Ag nanoparticles and TiO_2 makes it difficult to form a strong interfacial interaction, while the large contact interface between the small Cu or Cu–Ag ASNCs and TiO_2 can enable a strong interaction.

In situ irradiated XPS was then performed to investigate the electron transfer direction during the photodeposition process, thus revealing the growth process of Cu–Ag ASNCs. For $Cu_{0.8}Ag_{0.2}/TiO_2$, under ultraviolet illumination (ultraviolet light was used in the photodeposition process), the BEs of Ag 3d and Cu 2p are negatively shifted by 0.2 and 0.4 eV, respectively, while the BE of Ti 2p is positively shifted by 0.3 eV, indicating that the photogenerated electrons on TiO_2 migrate to Cu and Ag during the photodeposition process. Based on the above results, we propose the following mechanism for the photodeposition processes. Under ultraviolet illumination, the electrons generated in TiO_2 are enriched in the photogenerated electron flow sites and react

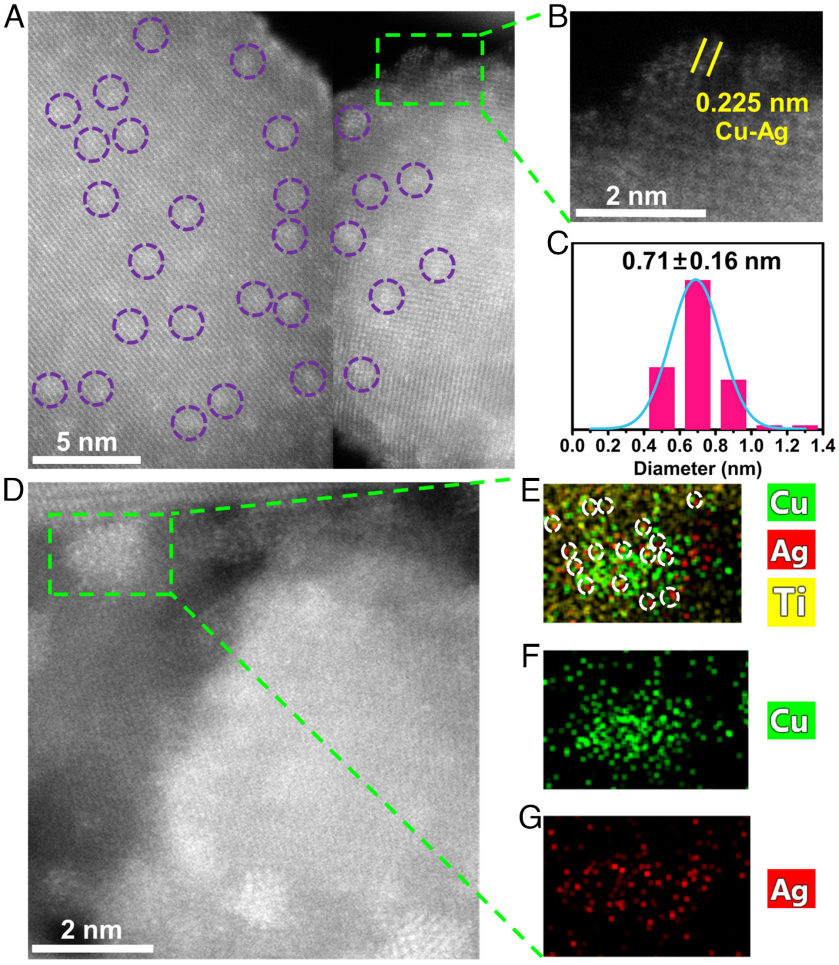

Fig. 1. The microstructure of the catalyst. (*A* and *B*) HAADF-STEM images of $Cu_{0.8}Ag_{0.2}/TiO_2$. Size distributions (*C*) and TEM elemental mapping images (*D* and *E*–*G*) of Cu–Ag ASNCs. The size distribution of Cu–Ag ASNCs was obtained by counting 58 particles in Fig. 1 and *SI Appendix*, Fig. S3, with the "Nano Measurer" tool. The bright colored areas are sub-nanoclusters, and the dark colored areas are TiO_2 carriers.

with Cu^{2+} to form Cu/TiO_2 (40). The photogenerated electrons generated in TiO_2 are then enriched on the surface of Cu and then react with Ag^+ added to the suspension later. Since the reduction potential of Cu is much lower than that of Ag, the deposition rate of Cu is much slower than that of Ag. Therefore, the deposition time of 30 min is not sufficient to deposit all the Cu^{2+} on the surface of TiO_2, and the residual Cu^{2+} is further deposited on the surface of Ag, thus forming a Cu–Ag alloy. It is worth noting that during the photodeposition process, the Cu–Ag alloy is deposited on the photogenerated electron flow sites of TiO_2 (40, 41), which is more favorable for the migration of photogenerated electrons of TiO_2 to the Cu–Ag alloy, thus helping to avoid the oxidation of Cu–Ag alloy as active sites during the CO_2 photoreduction process.

UV–Vis DRS spectrum was used to study the SPR effect of metal cocatalysts, and the results are presented in *SI Appendix*, Fig. S5*B*. The Ag/TiO_2 shows a strong SPR absorption peak under visible light, while Cu/TiO_2 does not display an obvious SPR absorption peak (*SI Appendix*, Fig. S5*B*). This is due to the reduction of the SPR effect with the decrease of the metal particle size within a certain range (42), and the particles of Ag in Ag/TiO_2 are much larger than the particles of Cu in Cu/TiO_2, which leads to a much higher SPR effect of Ag/TiO_2 than Cu/TiO_2. For Cu_xAg_{1-x}/TiO_2, the SPR intensity decreases with the increase of Cu content, which may be due to the decrease of the particle size of the Cu–Ag alloy with the increase of Cu content. In addition, the absorption intensity of visible light by $Cu_{0.8}Ag_{0.2}/TiO_2$ is very weak, indicating that the SPR effect of $Cu_{0.8}Ag_{0.2}/TiO_2$ is not obvious, which is because the Cu–Ag ASNCs in $Cu_{0.8}Ag_{0.2}/TiO_2$ are smaller than the lower limit for producing the SPR effect.

CO_2 Photoreduction Performance of Catalysts and Isotope Labeling for C and O. The activity of catalysts for photocatalytic conversion of CO_2 and H_2O was evaluated under AM 1.5G simulated solar irradiation, and the results are presented in Fig. 3. As shown in Fig. 3*A*, TiO_2 exhibits very low CO_2 photoreduction activity, probably due to its weak absorption of solar light and its lack of active sites for reaction with CO_2. However, the CO_2 photoreduction activity of TiO_2 is significantly enhanced when loaded with Ag nanoparticles or Cu sub-nanoclusters, which can be ascribed to the enhanced visible light absorption via the SPR effect of Ag or the promotion of CO_2 activation by Cu as the active site. The CO_2 photoreduction activity of Cu_xAg_{1-x}/TiO_2 ($x = 0.2$, 0.4, 0.6, 0.8) is much higher than that of Cu/TiO_2 and Ag/TiO_2. In a certain range ($x \le 0.6$), the formation rates of CH_4 and C_2H_4 increase with increasing Cu content. This is because the size of the Cu–Ag alloy decreases with increasing Cu content, which leads to an increase in the number of active sites. In addition, as the size of Cu–Ag alloy decreases, the interaction between Cu–Ag alloy and TiO_2 is enhanced and the IFS are gradually formed, which can generate hot electrons to participate in CO_2 reduction reaction under visible light. The formation rate of C_2H_4 on $Cu_{0.8}Ag_{0.2}/TiO_2$ is much higher than that on other catalysts, while the formation rate of CH_4 on $Cu_{0.8}Ag_{0.2}/TiO_2$ is lower than that on $Cu_{0.6}Ag_{0.4}/TiO_2$. This is possibly because the C–C coupling of the intermediates and the desorption of C_2H_4* has reached an optimal balance on the $Cu_{0.8}Ag_{0.2}/TiO_2$ catalyst, thereby increasing the

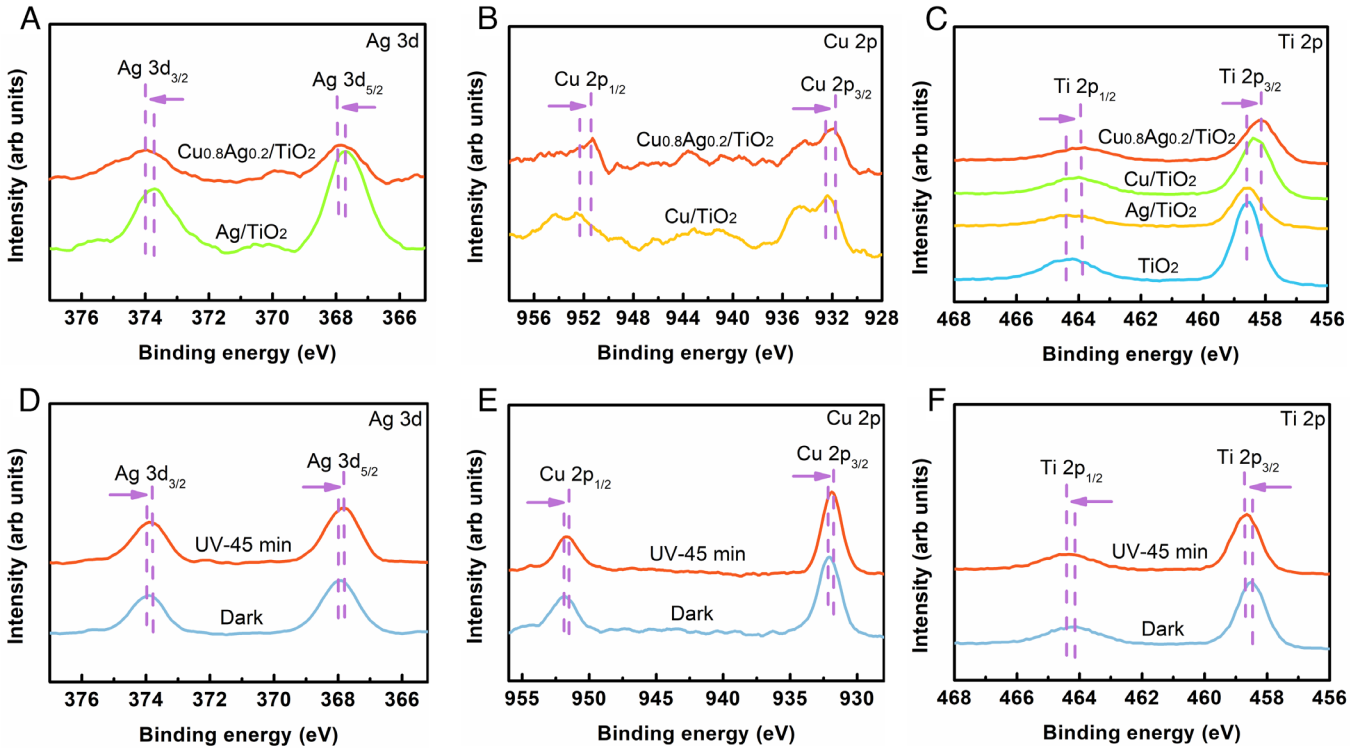

Fig. 2. Characterization of the composition and photogenerated electron migration direction of catalysts. XPS spectra for Ag 3d (*A*), Cu 2p (*B*), and Ti 2p (*C*) of the catalysts. In situ irradiated XPS spectra for Ag 3d (*D*), Cu 2p (*E*), and Ti 2p (*F*) of $Cu_{0.8}Ag_{0.2}/TiO_2$ in the dark or under ultraviolet irradiation.

selectivity of C_2H_4 and reducing the selectivity of CH_4. The C_2H_4 formation rate on $Cu_{0.8}Ag_{0.2}/TiO_2$ (1110.6 ± 82.5 μmol g^{-1} h^{-1}) is record-high with an order-of-magnitude enhancement relative to current work on photocatalytic conversion of CO_2 and H_2O for C_2H_4 photosynthesis (*SI Appendix,* Table S2), which makes sunlight-powered synthesis of C_2H_4 more realistic on an industrial scale. Moreover, the selectivity of C_2H_4 is as high as 49.1 ± 1.9% (Fig. 3*B* and *SI Appendix,* Table S3), which is higher than most of the reported selectivity of C_2H_4, indicating that the Cu–Ag ASNCs can effectively improve both the activity and the selectivity

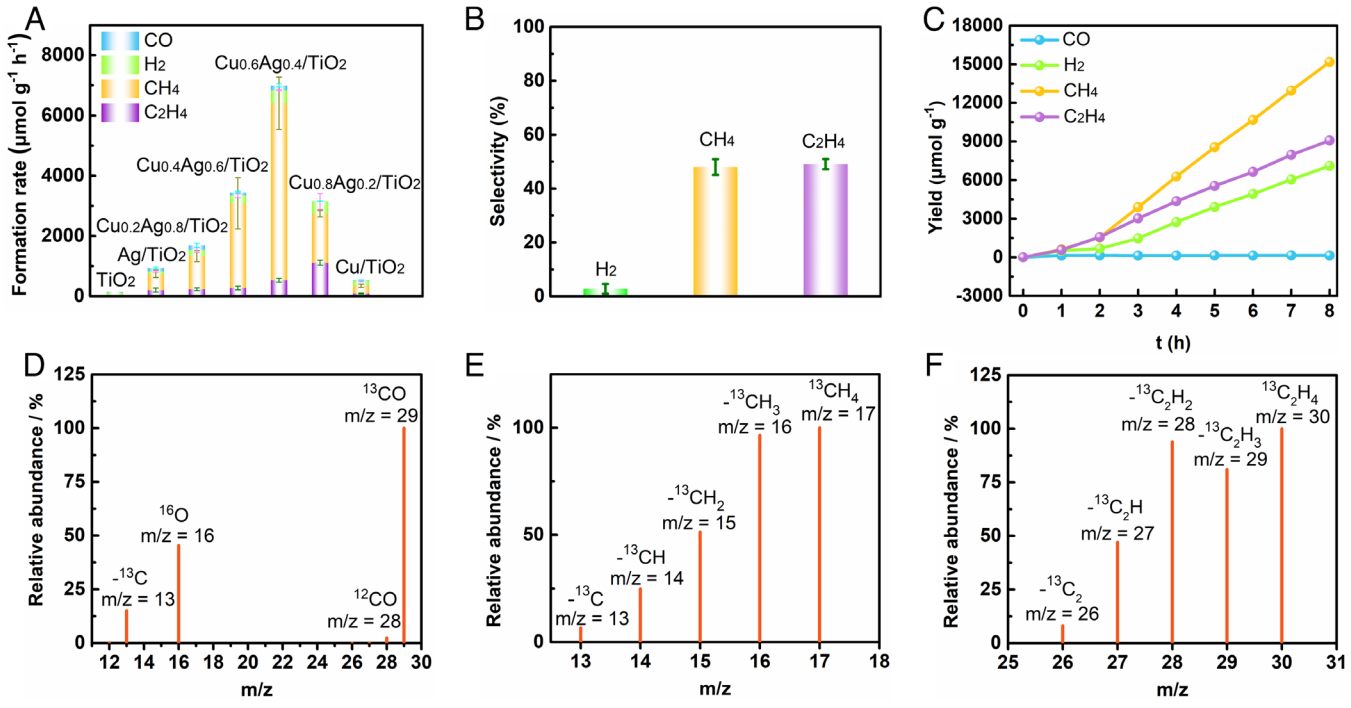

Fig. 3. Evaluation of photocatalytic performance. (*A*) C_2H_4, CH_4, H_2, and CO formation rates of the catalysts after 8-h simulated sunlight (AM1.5G) irradiation. (*B*) The selectivity of C_2H_4, CH_4, and H_2 on $Cu_{0.8}Ag_{0.2}/TiO_2$. (*C*) Time-dependent C_2H_4, CH_4, H_2, and CO evolution over $Cu_{0.8}Ag_{0.2}/TiO_2$ in wet CO_2. Error bars were obtained by three independent photocatalytic measurements using $Cu_{0.8}Ag_{0.2}/TiO_2$. GC–MS spectra of CO (*D*), CH_4 (*E*), and C_2H_4 (*F*) from the photocatalytic reduction of $^{13}CO_2$ over $Cu_{0.8}Ag_{0.2}/TiO_2$.

for C_2H_4. In order to accurately evaluate the photocatalytic performance of the catalyst, we calculated the quantum efficiency of each reaction product over the $Cu_{0.8}Ag_{0.2}/TiO_2$ catalyst (see details in *SI Appendix*). In order to exclude the effect of catalyst amount on quantum efficiency calculations, we tested the C_2H_4 rate formation at different catalyst amount. As shown in *SI Appendix,* Fig. S6, the C_2H_4 formation rate does not increase linearly with increasing catalyst amount, which is consistent with other reports (24). This is because the CO_2 reduction reaction occurs at the surface of the catalyst, and an excess of catalyst is not favorable for catalytic performance. There is no significant difference between the C_2H_4 formation rate of a 10-mg catalyst and that of a 5-mg catalyst, so we chose the C_2H_4 formation rate of a 10-mg catalyst to calculate the quantum efficiency of C_2H_4. The quantum efficiencies of C_2H_4 over the $Cu_{0.8}Ag_{0.2}/TiO_2$ are 0.26 %, comparable to natural photosynthesis efficiency (43), which further demonstrates that the $Cu_{0.8}Ag_{0.2}/TiO_2$ catalyst can effectively photocatalytically reduce CO_2 to produce C_2H_4.

In order to investigate the effect of stepwise photodeposition methods on the photocatalytic activity of the catalysts, we prepared the catalysts using impregnation (44) and co-photodeposition methods (45–47) and tested their photocatalytic activity. As shown in *SI Appendix,* Fig. S7*A*, the catalytic performance of $Cu_{0.8}Ag_{0.2}/TiO_2$ prepared using the impregnation method is much lower than that of $Cu_{0.8}Ag_{0.2}/TiO_2$ prepared using the stepwise photodeposition method, which may be due to the fact that the deposition positions of Cu^+ and Ag^+ are random and it is difficult to form Cu–Ag alloy effectively. Since the synergistic effect of Cu and Ag in Cu–Ag alloy is the key to C_2H_4 production, it is also difficult to effectively photocatalytically reduce CO_2 to produce C_2H_4 using $Cu_{0.8}Ag_{0.2}/TiO_2$ prepared by the impregnation method. As shown in *SI Appendix,* Fig. S7*B*, the catalytic performance of $Cu_{0.8}Ag_{0.2}/TiO_2$ prepared using the co-photodeposition method is much lower than that of $Cu_{0.8}Ag_{0.2}/TiO_2$ prepared using the stepwise photodeposition method; this is mainly due to the easy formation of core–shell structure between Cu and Ag in this process. In addition, some other drawbacks of this preparation process also limit its photocatalytic performance (*SI Appendix, The Method of Stepwise Photodeposition Reported in this Work Differs from Other Photodeposition Methods*).

The variation of yield of each product on $Cu_{0.8}Ag_{0.2}/TiO_2$ with time was studied, and the results are shown in Fig. 3*C*. The formation rates of C_2H_4, CH_4, and H_2 increase with increasing reaction time during the first 2 h, probably because the photogenerated electrons reduce a small amount of Cu^+ in the Cu–Ag ASNCs to Cu, thus activating the photocatalytic activity. However, when the reaction time exceeds 2 h, the formation rates of C_2H_4, CH_4, and H_2 remain unchanged, indicating an excellent stability of $Cu_{0.8}Ag_{0.2}/TiO_2$. In addition, the formation rates of CH_4 and C_2H_4 are the same during the first 2 h, while after 2 h, the formation rate of CH_4 becomes higher than that of C_2H_4. This may be because the Cu^+ in the Cu–Ag alloy reduces the selectivity of CH_4, and with the increase of reaction time, the Cu^+ is reduced to Cu^0, thus increasing the selectivity of CH_4. To further evaluate the photocatalytic stability of the $Cu_{0.8}Ag_{0.2}/TiO_2$, the photocatalytic recycling tests were carried out. As shown in *SI Appendix,* Fig. S8, the yield of various products varies insignificantly from the first cycle to the third cycle, further demonstrating the high stability of the $Cu_{0.8}Ag_{0.2}/TiO_2$ catalyst, which is attributed to the fact that there is no significant growth of the Cu–Ag alloy sub-nanoclusters after the CO_2 reduction reaction (*SI Appendix,* Fig. S9). Moreover, no C_2H_4 is produced in the control experiments conducted in argon and H_2O (*SI Appendix,* Fig. S10), indicating that the carbon element in C_2H_4 is derived from CO_2.

The experiment using isotope-labeled $^{13}CO_2$ was also conducted. The mass spectra of CO (Fig. 3*D*), CH_4 (Fig. 3*E*), and C_2H_4 (Fig. 3*F*) products are similar to those of the standard ^{13}CO, $^{13}CH_4$, and $^{13}C_2H_4$, indicating that the carbon element in the CO, CH_4, and C_2H_4 products is mainly from CO_2. In addition, the total yield of C_2H_4 and CH_4 is 1.03 mg after 8 h of reaction, while the catalyst used is only 2.0 mg (*SI Appendix,* Table S4). Such high yields of C_2H_4 and CH_4 also suggest that the carbon element in C_2H_4 arises from CO_2 rather than organic species adsorbed on the surface of TiO_2. O_2 can also be detected, however, because the reaction system cannot achieve absolute air tightness, resulting in O_2 in the air entering the reaction system, thus it cannot be determined whether some of the O_2 comes from the oxidation of H_2O. Therefore, the isotope tracer control experiment using $H_2{}^{18}O$ and CO_2 was also conducted to determine the source of O in O_2, and the results are shown in *SI Appendix,* Fig. S11. There are $^{16}O^{16}O$, $^{16}O^{18}O$ and $^{18}O^{18}O$ peaks in *SI Appendix,* Fig. S11*A* and the relative abundance of $^{16}O^{16}O$ is much higher than that of $^{16}O^{18}O$ and $^{18}O^{18}O$. This is because the O_2 in the reactor cannot be completely removed, and the O_2 in the air enters the reactor during the reaction process, which leads to the enhancement of $^{16}O^{16}$ relative abundance. The relative abundance of $^{16}O^{18}O$ is much higher than that of $^{18}O^{18}O$. This is because $^{18}O^{18}O$ formed by the oxidation of $H_2{}^{18}O$ by photogenerated holes can undergo rapid oxygen isotope exchange with $^{16}O^{16}O$, resulting in a higher relative abundance of $^{16}O^{18}O$ (48, 49). In addition, the relative abundance of $^{16}O^{18}O$ increases significantly after 16 h of irradiation (*SI Appendix,* Fig. S11*B*) relative to 11 h of irradiation (*SI Appendix,* Fig. S11*A*), indicating that the content of $^{16}O^{18}O$ increases with increasing irradiation time, which further suggests that the ^{18}O in $^{16}O^{18}O$ comes from the oxidation of $H_2{}^{18}O$. The relative abundance of $^{18}O^{18}O$ increases slightly with increasing irradiation time, which is because most of the $^{18}O^{18}O$ undergo oxygen isotope exchange with $^{16}O^{16}O$ to reach a equilibrium of oxygen isotope exchange.

Identification of the Interface States. The IFS generated by TiO_2 and Ag nanoclusters play an important role in the CO_2 photoreduction reaction, so we investigated the IFS generated by Cu–Ag metal nanoclusters and TiO_2 by density functional theory (DFT) calculations. The projected density of states (PDOS) of TiO_2 shows a band gap in which valence and conduction bands are mainly formed by O 2p and Ti 3d orbitals, respectively (*SI Appendix,* Fig. S12*A*). Notably, Ag/TiO_2 exhibits the formation of the IFS in the band gap region (Fig. 4*A*), which is in a good agreement with previous studies (28, 29). The IFS of Ag/TiO_2 can be attributed to the charge donation from Ag 5 s to O 2p of neighboring atoms and Ti 3d orbitals (Fig. 4*D*) (29). According to reports, the hot electrons generated in the IFS under visible light are consistent with ultrafast (<10 fs) photoinduced hot electrons in TiO_2, rather than electrons photogenerated in Ag nanoclusters (28). This suggests that the hot electrons used for CO_2 reduction under simulated sunlight originate from TiO_2 at the IFS rather than from the SPR effect of Ag. The hot electrons generated in TiO_2 may rapidly migrate to the neighboring Ag sub-nanoclusters to participate in the CO_2 reduction reaction (29). Cu/TiO_2 also shows an IFS in the band gap region (Fig. 4*B*), which is attributed to the charge donation from Cu 3d to O 2p of neighboring atoms and Ti 3d orbitals (Fig. 4*E*). The PODOS of Cu–Ag alloy/TiO_2 only exhibits the IFS generated by the interaction of Cu 3d with TiO_2 (Fig. 4 *C* and *F*), probably because the intensity of IFS in Cu/TiO_2 is much higher than that of Ag/TiO_2, thus the IFS signal of Ag/TiO_2 is negligible. After amplifying the PDOS signals of Ag 5 s, Ag 4p, and Ag 4d of Cu–Ag alloy/TiO_2, the signals

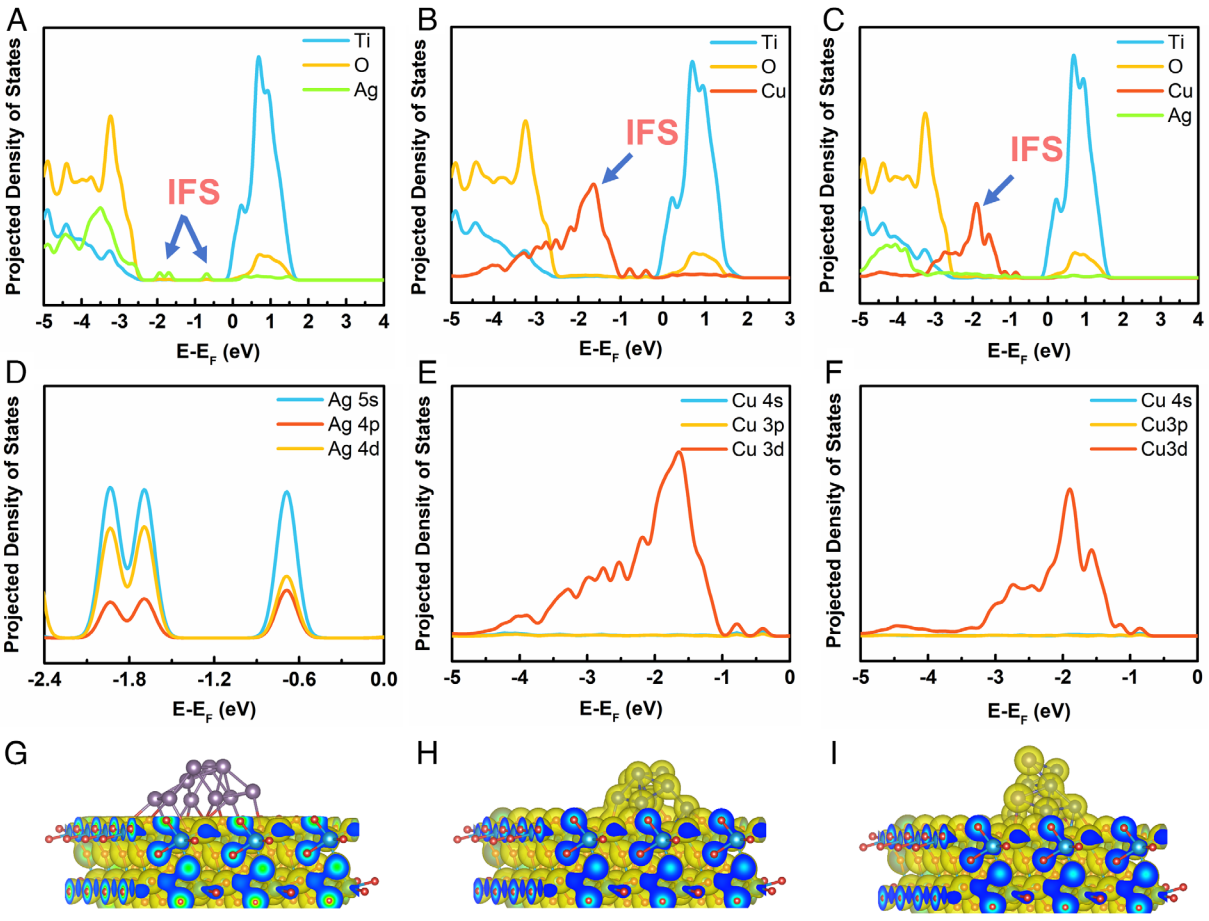

Fig. 4. DFT calculation results of IFS. The projected density of states (PDOS) for Ag/TiO_2 (*A*), Cu/TiO_2 (*B*), and Cu–Ag alloy/TiO_2 (*C*). (*D*) The PDOS for Ag 5 s, Ag 4p, and Ag 4d of Ag/TiO_2. The PDOS for Cu 4 s, Cu 3p, and Cu 3d of Cu/TiO_2 (*E*) and Cu–Ag alloy/TiO_2 (*F*). Partial charge density for the IFS of Ag/TiO_2 (*G*), Cu/TiO_2 (*H*), and Cu–Ag alloy/TiO_2 (*I*). The isosurface level is 0.05 e/Å^3. Ti, O, Cu, and Ag atoms are blue, red, gray blue, and violet, respectively.

of IFS in Ag–TiO_2 interactions can be observed (*SI Appendix,* Fig. S12*B*), indicating that IFS of Ag/TiO_2 still exists in Cu–Ag alloy/TiO_2. In addition, compared to the IFS of Cu/TiO_2 (Fig. 4 *B* and *E*), the IFS of Cu–Ag alloy/TiO_2 is shifted to a higher level (Fig. 4 *C* and *F*), indicating that the interaction of Ag with Cu results in a stronger reduction capacity of the IFS in Cu–Ag alloy/TiO_2, which is favorable for the CO_2 photoreduction reaction. To further investigate the IFS of the catalyst, we select the IFS of the catalyst and performed a partial charge density calculation. The Ag nanoclusters at the IFS of Ag/TiO_2 only have a weak electron exchange with TiO_2 (Fig. 4*G*), while the Cu nanoclusters at Cu/TiO_2 have a strong electron exchange with TiO_2 (Fig. 4*H*), which is the reason why the IFS of Cu/TiO_2 is much stronger than that of Ag/TiO_2. It is noteworthy that both Cu and Ag at the IFS of Cu–Ag alloy/TiO_2 have a strong charge exchange with TiO_2 (Fig. 4*I*), which implies that the interaction between Cu and Ag could enhance the charge exchange between Ag and TiO_2. The values of the charge change (Δq) of Cu, Ag, and Cu–Ag sub-nanoclusters and TiO_2, calculated using the Bader method, are 1.89, 1.65, and 1.76 e, respectively, which is consistent with the results of Partial charge density. In summary, there is a strong IFS between Cu–Ag alloy nanoclusters and TiO_2, and the IFS originates from the charge exchange between Cu 3d/Ag 5 s and TiO_2. The visible light in simulated sunlight can excite the hot electrons of TiO_2 in the IFS which would transfer to the Cu–Ag alloy nanoclusters to react with the CO_2, so the Cu–Ag alloy nanocluster acts as an electron acceptor rather than an electron donor in visible light, which is beneficial to the CO_2 photoreduction reaction.

Photoelectric and Reactant Adsorption Properties of Catalysts. The production and migration of photogenerated electrons are the key factors that determine the CO_2 photoreduction activity of catalysts. Therefore, TEMPO, which can capture photogenerated electrons (50), was used to measure the content of photogenerated electron on the catalyst surface under simulated sunlight, and the results are shown in *SI Appendix,* Fig. S13. After loading Cu and Ag on TiO_2, the consumption rate of TEMPO is accelerated, suggesting that Cu and Ag can observably boost the generation and migration of photogenerated electrons. Since Cu sub-nanoclusters have no SPR effect (*SI Appendix,* Fig. S5*B*), they mainly promote the separation of photogenerated electrons from photogenerated holes, while for Ag nanoparticles, they have a strong SPR effect (*SI Appendix,* Fig. S5*B*) and boost the production of photogenerated electrons. The TEMPO consumption on $Cu_{0.8}Ag_{0.2}/TiO_2$ is significantly faster than that on Cu/TiO_2 and Ag/TiO_2, indicating that $Cu_{0.8}Ag_{0.2}/TiO_2$ has a much higher ability to generate and separate photogenerated electrons than other catalysts. This is because the strong interfacial dielectric coupling between the Cu–Ag ASNCs and TiO_2 leads to the formation of the IFS, resulting in the direct generation of hot electrons in TiO_2 under visible light (28, 29), while the work function of Cu–Ag ASNCs (4.26–4.65 eV) is larger than that of TiO_2 (4.20 eV) (51, 52), leading to the rapid migration of these hot electrons to the surface of the Cu–Ag

ASNCs, thus increasing the surface electron density of the catalyst. In addition, the $Cu_{0.8}Ag_{0.2}/TiO_2$ can generate more superoxide and hydroxyl radicals than other catalysts (*SI Appendix*, Fig. S14), which further demonstrates that $Cu_{0.8}Ag_{0.2}/TiO_2$ can generate and separate the most photogenerated electrons and holes and that these photogenerated electrons and holes possess high enough reduction and oxidation potentials to participate in reduction and oxidation reactions.

DFT calculations were further carried out to investigate the electronic structure of catalysts to reveal the interactions between the individual components. The electronic location function (ELF, Fig. 5*A*) of Cu–Ag alloy/TiO_2 indicates that Cu–Ag ASNCs interact with TiO_2 in the form of covalent bonds, which can provide an efficient electronic channel for interfacial electron transfer between Cu–Ag ASNCs and TiO_2. In addition, the covalent bonding between the Cu–Ag ASNCs and TiO_2 indicates a strong interaction between them, which is consistent with the XPS results (Fig. 2*C*), revealing the essential reason for the formation of IFS at the interface of TiO_2 and Cu–Ag ASNCs. The charge difference distribution (Fig. 5*B*) reveals the electron transfer from Ag to Cu in the Cu–Ag ASNCs, which is consistent with the XPS results (Fig. 2 *A* and *B*). After loading Ag, the charge change value (Δq) of Cu calculated by the Bader analysis is −0.05 e, indicating that electrons in Ag tend to migrate toward Cu in the Cu–Ag alloy sub-nanoclusters.

The work function, a key parameter of the catalyst, was further used to study the migration direction of photogenerated electrons in the Cu–Ag ASNCs. The work function of Cu/TiO_2 (Fig. 5*C*) is 4.50 eV, which is between the work functions of Cu (4.65 eV) and TiO_2 (4.20 eV), and the work function of Ag/TiO_2 is 4.24 eV, which is between the work functions of Ag (4.26 eV) and TiO_2 (4.20 eV). The change of Fermi energy and work function between the two components further indicates the strong interfacial interaction between Cu/Ag and TiO_2. The work function of Cu–Ag alloy/TiO_2 (4.39 eV, Fig. 5*E*) is lower than that of Cu/TiO_2 (4.50 eV, Fig. 5*C*) but higher than that of Ag/TiO_2 (4.24 eV, Fig. 5*D*), implying that the electrons could flow from Ag to Cu in Cu–Ag ASNCs. All these results reveal that electrons could migrate from Ag to Cu in the Cu–Ag ASNCs, which suggests that electrons will accumulate on Cu under solar light, and therefore, Cu is most likely to be the active site for the CO_2 reduction reaction.

The accumulation of photogenerated electrons on the Cu surface in the Cu–Ag ASNCs cannot be used as direct evidence to prove that Cu is the active site in the CO_2 photoreduction process. This is because the adsorption of CO_2 on the catalyst is also crucial. Therefore, the adsorption performance of CO_2 on metal cocatalysts was investigated by DFT calculations. The initial structures before optimization of CO_2 molecules adsorbed on Cu–Ag alloy/TiO_2 are shown in *SI Appendix*, Fig. S15, and the structure after optimization is shown in Fig. 5 *F*–*I*. For the adsorption of CO_2 on Cu/TiO_2 or Ag/TiO_2, before structure optimization, C and O in CO_2 are placed at the same distance from Cu (*SI Appendix*, Fig. S15*C*) or Ag (*SI Appendix*, Fig. S15*D*). When the structure is optimized, O in CO_2 will be adsorbed on Cu (Fig. 5*H*) or Ag

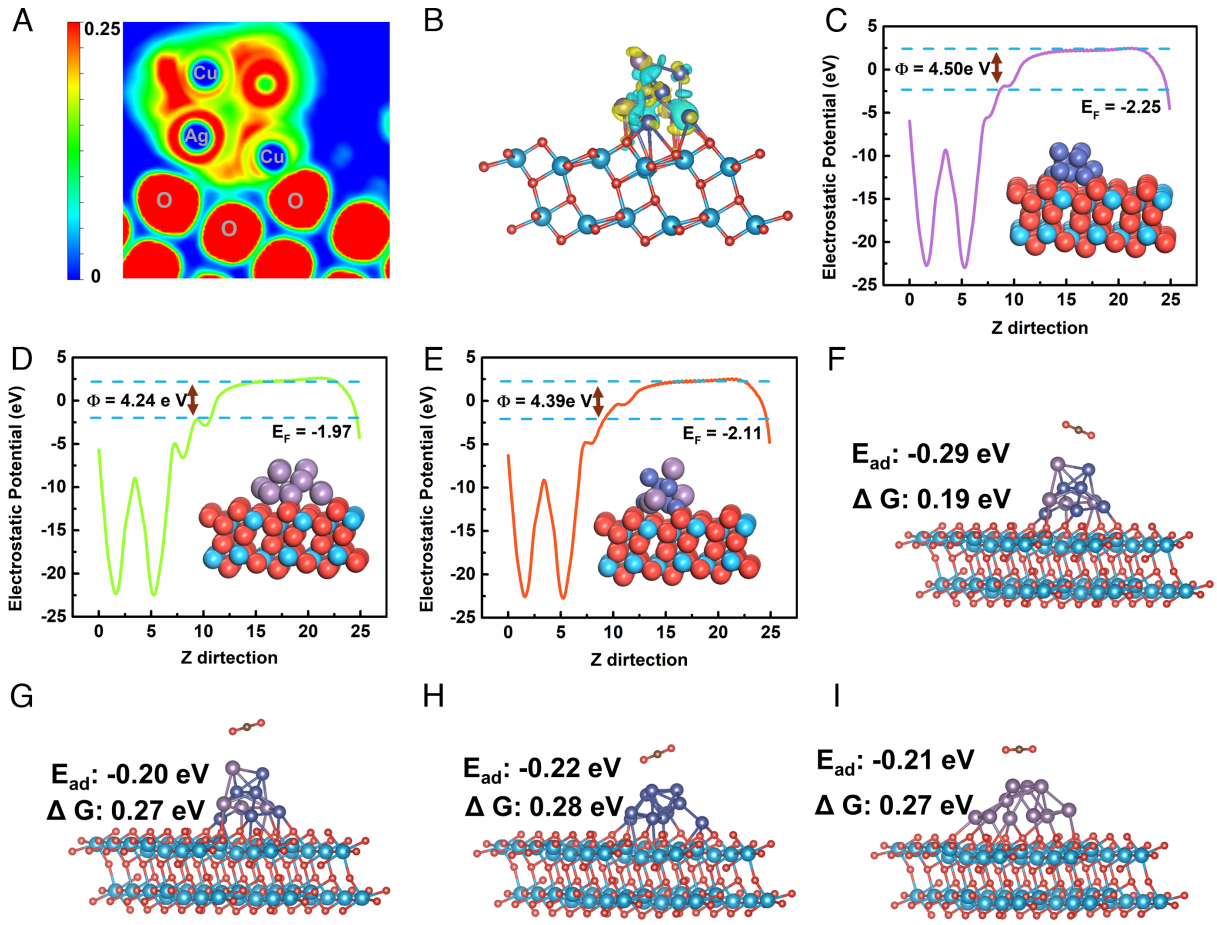

Fig. 5. DFT calculation results. (*A*) The ELF of Cu–Ag alloy/TiO_2. (*B*) The charge difference distribution between Cu and Ag; charge accumulation is in blue and depletion is in yellow. The isosurface level is 0.005 e/Å^3. The calculated electrostatic potentials for Cu/TiO_2 (*C*), Ag/TiO_2 (*D*), and Cu–Ag alloy/TiO_2 (*E*). Optimized structures of CO_2 molecules adsorbed on Cu in Cu–Ag alloy/TiO_2 (*F*), Ag in Cu–Ag alloy/TiO_2 (*G*), Cu in Cu/TiO_2 (*H*), Ag in Ag/TiO_2 (*I*), and their adsorption energies and Gibbs free energies. Ti, O, Cu, Ag, and C atoms are blue, red, gray blue, violet, and brown spheres, respectively.

(Fig. 5*I*), indicating that O in CO_2 is more easily adsorbed on the surface of Cu or Ag. For the adsorption of CO_2 on Cu–Ag alloy/TiO_2, the distance of CO_2 from Cu and Ag in the initial structure is the same (*SI Appendix,* Fig. S15*A*), and when the structure is optimized, CO_2 will be adsorbed on Cu (Fig. 5*F*), which indicates that CO_2 is more easily adsorbed on Cu. The CO_2 adsorption energy (E_{ad}) on Cu sites in Cu–Ag alloy/TiO_2 (−0.29 eV, Fig. 5*F* and *SI Appendix,* Table S5) is much higher than that on Ag sites (−0.20 eV, Fig. 5*G* and *SI Appendix,* Table S5), suggesting that CO_2 has stronger adsorption stability on Cu sites in Cu–Ag ASNCs. In addition, the Gibbs free energies (ΔG) of CO_2 adsorption on Cu sites in Cu–Ag alloy (0.19 eV, Fig. 5*F* and *SI Appendix,* Table S5) is lower than that on Ag sites (0.27 eV, Fig. 5*G* and *SI Appendix,* Table S5), indicating that CO_2 adsorption on the Cu sites requires lower energy expenditure than that on the Ag sites. The above results combined with the results of the flow direction of photogenerated electrons demonstrate that Cu is the active site for the CO_2 photoreduction process in the Cu–Ag ASNCs. The CO_2 adsorption energy on Cu–Ag alloy/TiO_2 (−0.29 eV, Fig. 5*F*) is much higher than that on Cu/TiO_2 (−0.22 eV, Fig. 5*H*) and Ag/TiO_2 (−0.21 eV, Fig. 5*I*), indicating that the interaction between Cu and Ag in the Cu–Ag ASNCs can enhance the stability of CO_2 adsorption on the catalyst. The CO_2 adsorption Gibbs free energy on Cu–Ag alloy/TiO_2 (0.19 eV, Fig. 5*F*) is lower than that on Cu/TiO_2 (0.28 eV, Fig. 5*H*) and Ag/TiO_2 (0.27 eV, Fig. 5*I*), indicating that the interaction between Cu and Ag in the Cu–Ag ASNCs can reduce the energy expenditure of CO_2 adsorption on the catalyst surface.

Reaction Pathway and C–C Coupling Mechanism. In situ FT-IR spectra were used to investigate the reaction intermediates in the photocatalytic CO_2 reduction to determine the reaction pathways (50–52). As shown in Fig. 6*A*, the adsorption of CO_2 and H_2O on the $Cu_{0.8}Ag_{0.2}/TiO_2$ surface induces the formation of bidentate carbonate (b-CO_3^{2-}, at 1,366 cm^{-1}), monodentate carbonate (m-CO_3^{2-}, at 1,536 and 1,296), H_2O* (at 1,636 cm^{-1}), and bicarbonate (HCO^{3-}, at 1,430 cm^{-1}) (19, 24, 53–55). The intensities of the adsorption peaks of CO_2 on Ag/TiO_2 (Fig. 6*D*) and TiO_2 (*SI Appendix,* Fig. S16) are significantly weaker than that on Cu/TiO_2 (Fig. 6*C*), suggesting that CO_2 is mainly adsorbed on the Cu sites. The adsorption peak intensity of CO_2 on $Cu_{0.8}Ag_{0.2}/TiO_2$ (Fig. 6*A*) is slightly higher than that on Cu/TiO_2 (Fig. 6*C*), suggesting that the interaction between Ag and Cu in the Cu–Ag ASNCs significantly enhances the adsorption performance of CO_2 on Cu sites, which is in full agreement with the results of DFT calculations (Fig. 5 *G* and *H*).

Under simulated sunlight, the surface of $Cu_{0.8}Ag_{0.2}/TiO_2$ shows a variety of reaction intermediates (Fig. 6 *A* and *B*), including CO_2^- (at 1,242 cm^{-1}), COOH* (at 1,211 and 1,580 cm^{-1}), HCOOH* (at 1,343 cm^{-1}), CHO* (at 1,714 cm^{-1}), CH_2* (at 1,480 cm^{-1}), CH_3* (at 1,395 cm^{-1}), and C_2H_4* (at 1,442 and 1,693 cm^{-1}) (30, 50, 56–61). The C_2H_4* reaction intermediate indicates the formation of C_2H_4. The formation of CH_2* intermediate indicates that C_2H_4* is derived from a C–C coupling of CH_2*. No reaction intermediates are detected on TiO_2 under simulated sunlight, which can be ascribed to the difficulty of CO_2 to adsorb on the TiO_2 surface (*SI Appendix,* Fig. S16). Only CO^{2-} and COOH* intermediates are detected on Ag/TiO_2 under simulated sunlight (Fig. 6*D*). This is probably because the conversion of CO^{2-} and COOH* to HCOOH* requires a large energy input, thus preventing the proceeding of the subsequent reactions. The species of reaction intermediates on Cu/TiO_2 (Fig. 6*C*) are analogous to those on $Cu_{0.8}Ag_{0.2}/TiO_2$ (Fig. 6 *A* and *B*), but no C_2H_4* intermediates are observed on Cu/TiO_2, suggesting that Cu sub-nanoclusters cannot promote the C–C coupling of CH_2* intermediates and that the interaction between Cu and Ag in the of Cu–Ag ASNCs is the key to the production of C_2H_4.

Based on the above results, the photocatalytic conversion pathway of CO_2 and H_2O on $Cu_{0.8}Ag_{0.2}/TiO_2$ to produce C_2H_4 is proposed as follows. The asterisks (*) denote catalytically active

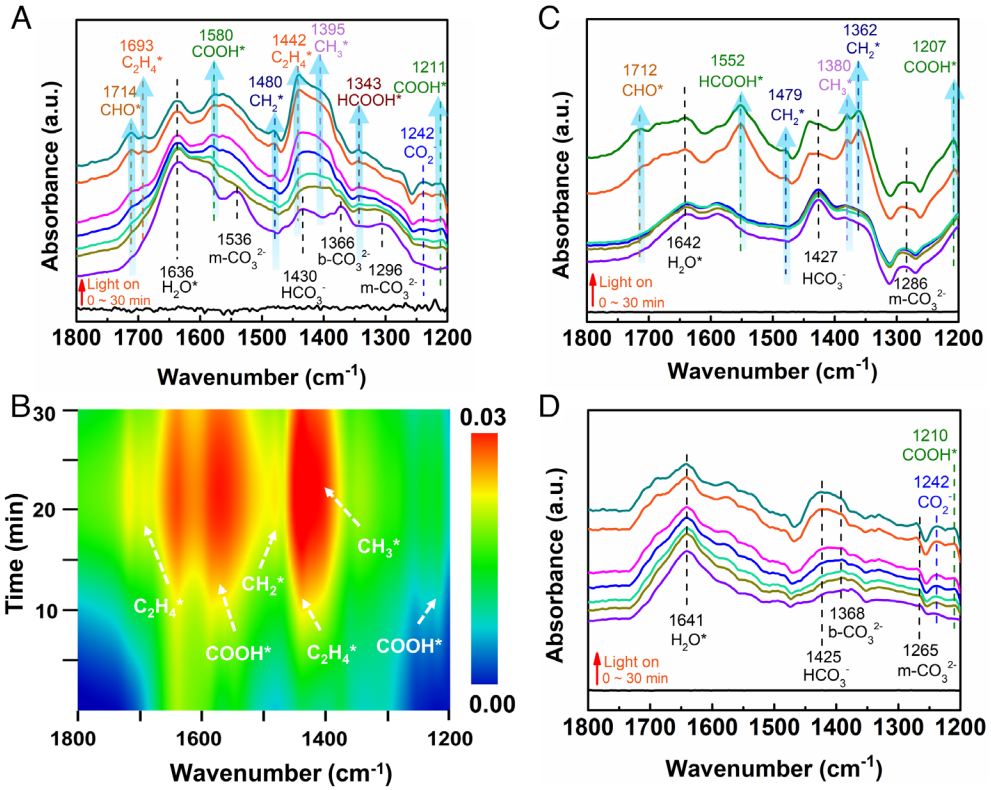

Fig. 6. In situ FT-IR spectra for CO_2 photoreduction process. In situ FT-IR spectra of CO_2 and H_2O interaction with $Cu_{0.8}Ag_{0.2}/TiO_2$ (*A*) and its corresponding contour projection (*B*). In situ FT-IR spectra of CO2 and H2O interaction with Cu/TiO_2 (*C*), Ag/TiO_2 (*D*). The curves from bottom to top represent background, adsorption for 30 min, and illumination for 2, 4, 6, 10, 20, and 30 min, respectively.

sites and the vertical arrows represent the release of gas product in the reaction.

$$CO_2^* + e^- + H^+ \rightarrow COOH^* \quad [1]$$

$$COOH^* + e^- + H^+ \rightarrow HCOOH^* \quad [2]$$

$$HCOOH^* + e^- + H^+ \rightarrow CHO^* + H_2O \quad [3]$$

$$CHO^* + e^- + H^+ \rightarrow HCHO^* \quad [4]$$

$$HCHO^* + e^- + H^+ \rightarrow CH_2OH^* \quad [5]$$

$$CH_2OH^* + e^- + H^+ \rightarrow CH_2^* + H_2O \quad [6]$$

$$C_2H_4^* \rightarrow C_2H_4 \uparrow \quad [7]$$

$$C_2H_4^* \rightarrow C_2H_4 \uparrow \quad [8]$$

Based on the reaction pathway proposed by the in situ FT-IR results, Gibbs free energy calculations were conducted to study the effect of Cu–Ag ASNCs on the key steps of C–C coupling and C_2H_4* desorption during the CO_2 reduction reaction. For the Cu/TiO_2 (Fig. 7*A*), the hydrogenation of CH_2* to produce CH_3* releases 1.03 eV of energy, while the C–C coupling of CH_2* to produce C_2H_4* requires 0.20 eV of energy expenditure, suggesting that the hydrogenation of CH_2* on Cu/TiO_2 to produce CH_3* is a spontaneous process, while the C–C coupling of CH_2* to produce C_2H_4* on Cu/TiO_2 involves a large activation energy barrier. Since the hydrogenation of CH_2* to produce CH_3* and the C–C coupling of CH_2* to produce C_2H_4* is a competing reaction, the conversion of CH_2* to CH_3* inhibits the production of C_2H_4*, which is the reason that Cu/TiO_2 can produce a large amount of CH_4 but only a small amount of C_2H_4 in the CO_2 photoreduction reaction. The production of CH_3* and C_2H_4* from CH_2* on Ag/TiO_2 release energies of 1.20 and 0.90 eV, respectively (Fig. 7*B*), suggesting that the production of CH_3* and C_2H_4* from CH_2* on Ag/TiO_2 are both spontaneous processes.

However, the desorption of C_2H_4* from Ag/TiO_2 requires an energy expenditure of 1.61 eV (Fig. 7*B*), which means that C_2H_4* cannot be desorbed from the surface of Ag/TiO_2. As for the Cu–Ag alloy/TiO_2 (Fig. 7*C*), the production of CH_3* and C_2H_4* from CH_2* release energies of 1.05 and 0.58 eV, respectively, suggesting that the formation of CH_3* and C_2H_4* from CH_2* on Cu–Ag alloy/TiO_2 are both spontaneous processes. This is because the interaction between Cu and Ag in the Cu–Ag ASNCs promotes the C–C coupling of CH_2* at the Cu active site. In addition, the desorption of C_2H_4* from Cu–Ag alloy/TiO_2 requires an energy expenditure of 0.65 eV, which is much lower than the energy required for the desorption of C_2H_4* from Ag/TiO_2 (1.61 eV), suggesting that the interaction between Cu and Ag facilitates the desorption of C_2H_4*. To further explore whether C_2H_4 molecules on Cu–Ag alloys are more readily desorbed than C_2H_4 molecules on Ag, C_2H_4-TPD experiments over the Cu/TiO_2, Ag/TiO_2, and $Cu_{0.8}Ag_{0.2}$/TiO_2 were carried out. As shown in *SI Appendix*, Fig. S17, two C_2H_4 desorption peaks around 295 and 404 °C are observed over Ag/TiO_2, while lower C_2H_4-TPD desorption peaks are observed over Cu/TiO_2 (100, 228, and 341 °C) and $Cu_{0.8}Ag_{0.2}$/TiO_2 (100, 216, and 363 °C), which is consistent with the results

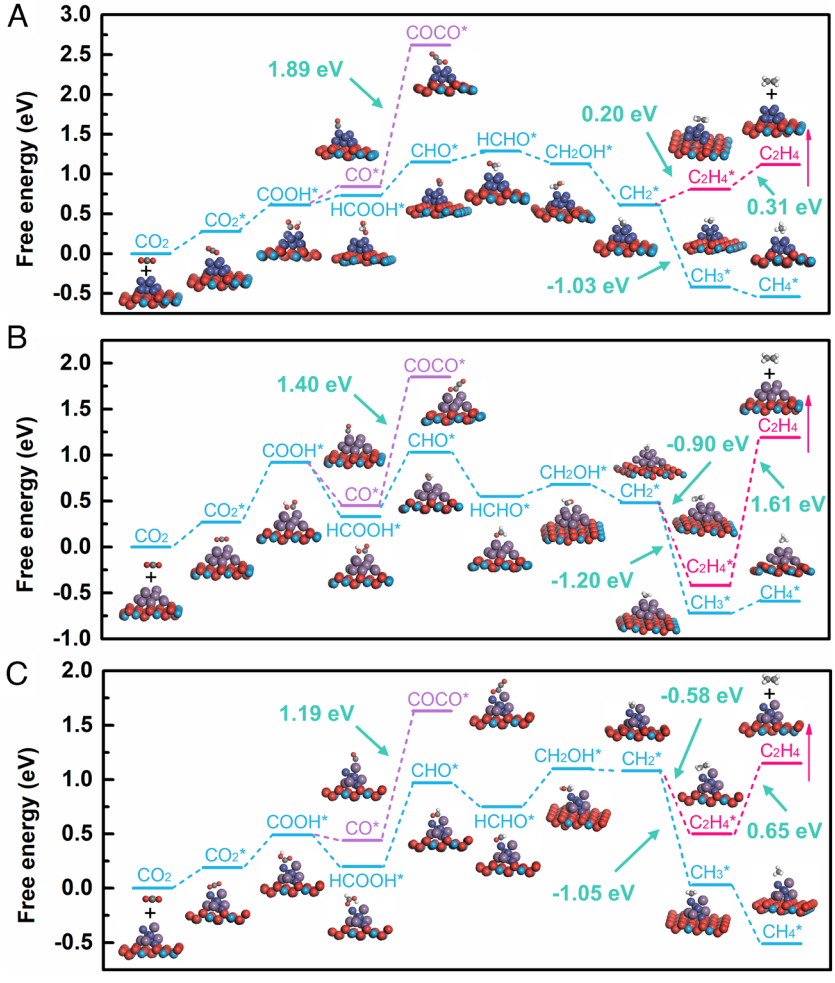

Fig. 7. Gibbs free energy calculations. Reaction pathways and C–C coupling step for CO_2 photoreduction on Cu/TiO_2 (*A*), Ag/TiO_2 (*B*), and Cu–Ag alloy/TiO_2 (*C*).

of DFT calculations, further indicating that the interaction between Cu and Ag facilitates the desorption of C_2H_4*. In short, the synergistic effect of Cu and Ag not only endows the Cu–Ag ASNCs with excellent C–C coupling properties like Ag but also with excellent C_2H_4 desorption properties like Cu, thus promoting the selective production of C_2H_4.

The C–C coupling between CH_2* and CH_2* or between CO* and CO* is generally considered a key step in the generation of C_2H_4 (62–66). Therefore, to determine the optimal C–C coupling pathway, the C–C coupling of CO* is also calculated even though no CO* intermediates are found in the in situ FT-IR spectra. The C–C coupling of CO* on Cu/TiO_2 (Fig. 7*A*), Ag/TiO_2 (Fig. 7*B*), and Cu–Ag alloy/TiO_2 (Fig. 7*C*) requires energy expenditures of 1.89, 1.40, and 1.19, respectively. Although the synergistic effect of Cu and Ag in the Cu–Ag ASNCs reduces the energy expenditure of C–C coupling of CO*, such a high energy expenditure still means that it is difficult for CO* to perform C–C coupling, confirming that C–C coupling of CH_2* is the key step for C_2H_4 production.

Based on the above results, the CO_2 photoreduction process on Cu–Ag ASNCs/TiO_2 is proposed in Fig. 8. The CO_2 adsorbs on Cu active sites of Cu–Ag ASNCs, and the interaction between Cu and Ag in the Cu–Ag ASNCs can effectively promote the adsorption of CO_2 on the Cu sites. Under solar irradiation, the ultraviolet light stimulates TiO_2 to produce photogenerated electrons, while the visible light stimulates the IFS at the contact interface of TiO_2 and Cu–Ag ASNCs to generate hot electrons. The photogenerated electrons and hot electrons rapidly migrate to the Cu active sites of Cu–Ag ASNCs to reduce the CO_2 adsorbed on the Cu active sites. The C–C coupling of CO* on Cu–Ag ASNCs/TiO_2 requires a huge energy expenditure, while the C–C coupling of CH_2* is a spontaneous process, suggesting that the C_2H_4 product comes from the C–C coupling of CH_2*. The CH_2* intermediates are unable to perform C–C coupling on Cu to produce C_2H_4*. Although CH_2* intermediates can perform C–C coupling on Ag, the C_2H_4* intermediates are difficult to be desorbed from the surface of Ag. However, the synergistic effect of Cu and Ag in Cu–Ag ASNCs not only promotes the C–C coupling of CH_2* to form C_2H_4* but also promotes the desorption of C_2H_4* from the catalyst, which are the key factors to promote the selective production of C_2H_4.

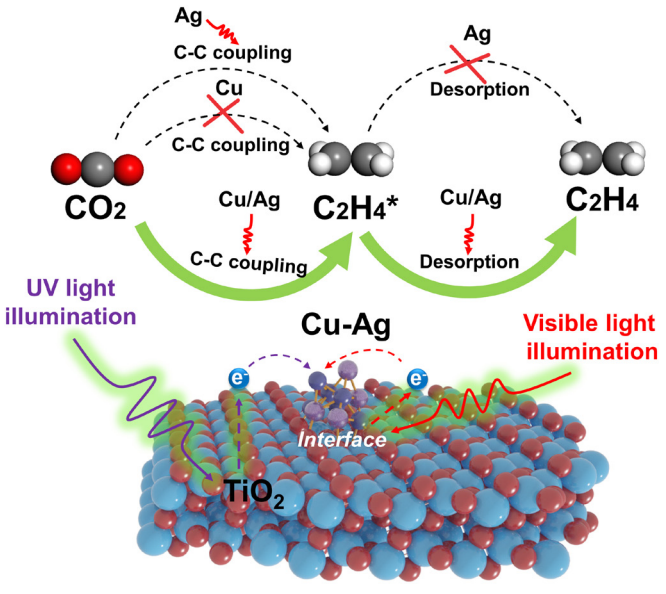

Fig. 8. Schematic illustration of photocatalytic conversion mechanism. CO_2 photoreduction process on Cu–Ag ASNCs/TiO_2. Ti, O, Cu, Ag, and C atoms are blue, red, gray blue, violet, and brown spheres, respectively.

Discussion

In conclusion, Cu–Ag ASNCs were loaded on TiO_2 through a facile stepwise photodeposition strategy. The strong interfacial dielectric coupling between the Cu–Ag ASNCs and TiO_2 leads to the formation of IFS, resulting in the direct generation of hot electrons in TiO_2 under visible light, which enhances the utilization of sunlight. The $Cu_{0.8}Ag_{0.2}/TiO_2$ demonstrates a record high C_2H_4 formation rate (1110.6 μmol g^{-1} h^{-1}), which is an order-of-magnitude enhancement relative to current work on photocatalytic conversion of CO_2 and H_2O for C_2 photosynthesis. CO_2 is more readily and stably adsorbed on Cu sites in Cu–Ag ASNCs, indicating that Cu in Cu–Ag ASNCs is the active site for CO_2 reduction reaction. The interaction between Cu and Ag in the Cu–Ag ASNCs can effectively promote the adsorption of CO_2 on the Cu sites. The difference in the work functions of Cu and Ag in the Cu–Ag ASNCs results in the migration of photogenerated electrons to the Cu active site, which facilitates the further reduction of CO_2 at the Cu active site. The results of in situ FT-IR spectra and DFT calculations indicate that the synergistic effect of Cu and Ag not only endows the Cu–Ag ASNCs with excellent C–C coupling properties like Ag but also with excellent C_2H_4* desorption properties like Cu, thus promoting selective production of C_2H_4. This work clarified the synergistic effect of Cu and Ag in the Cu–Ag ASNCs in the activation of CO_2, C–C coupling of CH_2* intermediates and C_2H_4* desorption from the catalyst, which provides a feasible strategy for photocatalytic conversion of CO_2 and H_2O to C_2 product.

Materials and Methods

Catalysts Preparation. Cu–Ag alloy sub-nanoclusters were deposited on TiO_2 via stepwise photodeposition which could avoid the formation of Ag/Cu core–shell structure. TiO_2 (P25, Degussa, 1.0 g) was added to absolute ethanol (150 mL) and sonicated for 10 min to form a suspension solution. Then, the solution was purged with N_2 for 30 min to remove the dissolved O_2. Variable volumes of Cu $(NO_3)_2.3H_2O$ (AR, Aladdin Chemical Reagent Co., Ltd.) precursor solution (5.0 mg/mL) were introduced into the above mixture and then illuminated under ultraviolet light for 30 min with stirring. Cu^{2+} was added only after the sample dispersion, and O_2 removal steps were completed, which avoided the impregnation of Cu^{2+} on the TiO_2 surface. Subsequently, variable volumes of $AgNO_3$ (AR, Aladdin Chemical Reagent Co., Ltd.) precursor solution (5.0 mg/mL) were also introduced into the above mixture and irradiated for another 30 min. The final suspension solution was centrifuged and washed with deionized water for five times. Finally, the catalysts were vacuum-dried at 80 °C for 24 h. The catalysts were denoted as Cu_xAg_{1-x}/TiO_2, where $x = 0$, 0.2, 0.4, 0.6, 0.8, and 1.0 corresponding to at % Cu. The quantum efficiency (QE%) of the catalysts was further calculated (see details in *SI Appendix*).

Catalyst Characterization. The high-angle annular dark field scanning transmission electron microscopy (HAADF-STEM) technique using a Titan 60-300 electron microscope (FEI Company, Netherlands) was used to observe the morphology and structure of the catalysts. The crystal phases of the catalysts were characterized by X-ray diffraction (XRD) patterns with CuK-α radiation (Model D/max RA, Rigaku Co.). The X-ray photoelectron spectroscopy (XPS) performed on a Thermo Scientific ESCALAB 250Xi X-ray photoelectron spectrometer was used to investigate the surface properties of the catalysts. The optical absorption properties were measured by UV-visible DRS (UV-2450, Shimadzu, Japan). Electron spin resonance (ESR) of electrons captured by 2,2,6,6-tetramethylpiperidin-1-oxyl (TEMPO) and radicals captured by 5,5-dimethyl-1-pyrroline N-oxide (DMPO) were conducted on a JES FA200 spectrometer. The C_2H_4-TPD experiments of the catalysts were tested on a temperature-programmed chemisorption instrument (Bel Cata II). Inductively coupled plasma optical emission spectroscopy (ICP-OES) experiments were performed using an Agilent 5110 spectrometer to determine the content of Cu and Ag in catalysts.

In Situ Irradiated XPS. In situ irradiated XPS was carried out with monochromatic Al Kα (1486.6 eV) radiation. The instrument model was an ESCALAB Xi^+

electron spectrometer (Thermo Scientific). The spectra were acquired in dark and after ultraviolet light for 45 min, respectively.

In Situ FT-IR Measurement. In situ FT-IR tests were carried out using the ConcentratIR 2™ (Harrick) on a Bruker Vertex 70v spectrometer equipped with an MCT detector. First, the loaded samples were processed in vacuum to remove the adsorbed H_2O for 30 min. Then, CO_2 and H_2O vapor were introduced into the reactor. After reaching the sorption equilibrium (30 min), the catalysts were irradiated under Xenon lamp (300 W, AM1.5 filter) for 30 min, and the FTIR spectra were recorded as a function of time to investigate the dynamics of the reduction of the reactants under irradiation.

CO_2 Photoreduction Tests. The photocatalytic CO_2 reduction tests were conducted in a Labsolar 6A closed circulation system (Beijing Perfectlight Technology Co., Ltd.). 2.0 mg catalyst dispersed in deionized water was uniformly loaded onto a glass fiber membrane (radius = 2.0 cm) by filtration. Subsequently, the reaction system was purged three times with high-purity CO_2 (99.99%) to remove the air in the reactor, and 150 μL of water was subsequently introduced to the reaction system. The pressure of the sealed reactor was maintained at 90 kPa. Finally, a 300-W Xenon lamp (Light intensity: 500 mW cm^{-2}) coupled with an AM 1.5G filter was used to irradiate the catalysts. During the irradiation, the gaseous products were analyzed per hour by a gas chromatography instrument. According to the required electrons in CO_2 reduction, the selectivity of C_2H_4 is evaluated: C_2H_4 selectivity (%) = $[12\varphi(C_2H_4)]/[12\varphi(C_2H_4) + 8\varphi(CH_4) + 2\varphi(CO) + 2\varphi(H_2)] \times 100\%$. After the reaction for 5 h, the catalyst was taken out and dried in vacuum at 80 °C, and then, the CO_2 reduction performance test was repeated three times to investigate the stability of the catalyst.

DFT Calculations. The ratio of Cu/Ag in Cu–Ag alloy sub-nanoclusters is modeled based on the results of HAADF-STEM images and TEM element mapping images. The elemental mapping analysis (Fig. 1 *D*–*G*) reveals that the content of Cu in Cu–Ag alloy sub-nanoclusters is slightly higher than that of Cu. The sub-nanoclusters are generally within 10 atoms, so we constructed a Cu–Ag sub-nanocluster containing 6 Cu atoms and 4 Ag atoms and ensured that the surface of the cluster contains both Cu and Ag atoms for comparison purposes. The "Vienna ab initio simulation package" (VASP5.4.1) was utilized to make the spin-polarized DFT calculations, which is based on the generalized gradient approximation with the Perdew–Burke–Ernzerhof (PBE) exchange and correlation functional (67–69). The Brillouin zone was sampled with a 3 × 3 × 1 K points. The structures were considered relaxed when all forces on each ion were smaller than 0.03 eV/Å, and the convergence criterion for the energy was 10^{-4} eV. The volume of exchanged electrons (Δq) was calculated using the Bader method. The Gibbs free energies in CO_2 photoreduction were calculated at 298.15 K, according to the equation $G = E_{DFT} + E_{ZPE} - TS$, where E_{DFT}, E_{ZPE}, and TS are the electronic energy, zero-point energy, and entropy contribution, respectively.

Data, Materials, and Software Availability. All study data are included in the article and/or *SI Appendix*.

ACKNOWLEDGMENTS. This work was supported by the National Natural Science Foundation of China (Grant Nos. 22225606 and 22261142663), Zhejiang Provincial Natural Science Foundation of China (Grant No. LZY23B030007), and Excellent Youth Foundation of Sichuan Scientific Committee Grant in China (No. 2021JDJQ0006).

1. H. Rao, L. C. S. Chmidt, J. Bonin, M. Robert, Visible-light-driven methane formation from CO_2 with a molecular iron catalyst. *Nature* **548**, 74–77 (2017).
2. C. Hepburn *et al.*, The technological and economic prospects for CO_2 utilization and removal. *Nature* **575**, 87–97 (2019).
3. Z. Guo *et al.*, Selectivity control of CO versus $HCOO^-$ production in the visible-light-driven catalytic reduction of CO_2 with two cooperative metal sites. *Nat. Catal.* **2**, 801–808 (2019).
4. C. Qian *et al.*, Catalytic CO_2 reduction by palladium-decorated silicon-hydride nanosheets. *Nat. Catal.* **2**, 46–54 (2019).
5. J. Li *et al.*, Self-adaptive dual-metal-site pairs in metal-organic frameworks for selective CO_2 photoreduction to CH_4. *Nat. Catal.* **4**, 719–729 (2021).
6. Z. Jiang *et al.*, Filling metal-organic framework mesopores with TiO_2 for CO_2 photoreduction. *Nature* **586**, 549–554 (2020).
7. L. Li *et al.*, Ethane/ethylene separation in a metal-organic framework with iron-peroxo sites. *Science* **362**, 443–446 (2018).
8. F. Jiao *et al.*, Shape-selective zeolites promote ethylene formation from syngas via a ketene intermediate. *Angew. Chem. Int. Ed.* **57**, 4692–4696 (2018).
9. L. Wang *et al.*, Thermally assisted photocatalytic conversion of CO_2-H_2O to C_2H_4 over carbon doped In_2S_3 nanosheets. *J. Mater. Chem. A* **8**, 10175–10179 (2020).
10. W. Wang *et al.*, Photocatalytic C-C coupling from carbon dioxide reduction on copper oxide with mixed-valence copper(I)/Copper (II). *J. Am. Chem. Soc.* **143**, 2984–2993 (2021).
11. M. B. Ross *et al.*, Designing materials for electrochemical carbon dioxide recycling. *Nat. Catal.* **2**, 648–658 (2019).
12. C. T. Dinh *et al.*, CO_2 electroreduction to ethylene via hydroxide-mediated copper catalysis at an abrupt interface. *Science* **360**, 783–787 (2018).
13. K. Jiang *et al.*, Metal ion cycling of Cu foil for selective C-C coupling in electrochemical CO_2 reduction. *Nat. Catal.* **1**, 111–119 (2018).
14. C. Choi *et al.*, Highly active and stable stepped Cu surface for enhanced electrochemical CO_2 reduction to C_2H_4. *Nat. Catal.* **3**, 804–812 (2020).
15. W. Ma *et al.*, Electrocatalytic reduction of CO_2 to ethylene and ethanol through hydrogen-assisted C-C coupling over fluorine-modified copper. *Nat. Catal.* **3**, 478–487 (2020).
16. L. Wan *et al.*, Cu_2O nanocubes with mixed oxidation-state facets for (photo) catalytic hydrogenation of carbon dioxide. *Nat. Catal.* **2**, 889–898 (2019).
17. Y. A. Wu *et al.*, Facet-dependent active sites of a single Cu_2O particle photocatalyst for CO_2 reduction to methanol. *Nat. Energy* **4**, 957–968 (2019).
18. J. Wang *et al.*, A single Cu-center containing enzyme-mimic enabling full photosynthesis under CO_2 reduction. *ACS Nano* **14**, 8584–8593 (2020).
19. Y. Li, B. Li, D. Zhang, L. Cheng, Q. Xiang, Crystalline carbon nitride supported copper single atoms for photocatalytic CO_2 reduction with nearly 100% CO selectivity. *ACS Nano* **14**, 10552–10561 (2020).
20. L. Yuan *et al.*, Dynamic evolution of atomically dispersed Cu species for CO_2 photoreduction to solar fuels. *ACS Catal.* **9**, 4824–4833 (2019).
21. Z. Jiang *et al.*, Living atomically dispersed Cu ultrathin TiO_2 nanosheet CO_2 reduction photocatalyst. *Adv Sci.* **6**, 1900289 (2019).
22. M. B. Gawande *et al.*, Cu and Cu-based nanoparticles: Synthesis and applications in catalysis. *Chem. Rev.* **116**, 3722–3811 (2016).
23. J. Wu, Y. Huang, W. Ye, Y. Li, CO_2 reduction: From the electrochemical to photochemical approach. *Adv. Sci.* **4**, 1700194 (2017).
24. S. t. Neaţu, J. A. Maciá-Agulló, P. Concepción, H. Garcia, Gold-copper nanoalloys supported on TiO_2 as photocatalysts for CO_2 reduction by water. *J. Am. Chem. Soc.* **136**, 15969–15976 (2014).
25. R. Long *et al.*, Isolation of Cu atoms in Pd lattice: Forming highly selective sites for photocatalytic conversion of CO_2 to CH_4. *J. Am. Chem. Soc.* **139**, 4486–4492 (2017).
26. X. Zhang *et al.*, Photocatalytic conversion of diluted CO_2 into light hydrocarbons using periodically modulated multiwalled nanotube arrays. *Angew. Chem. Int. Ed.* **51**, 12732–12735 (2012).
27. M. Y. Li *et al.*, Enhanced spatial light confinement of all inorganic perovskite photodetectors based on hybrid plasmonic nanostructures. *Small* **16**, 2004234 (2021).
28. S. Tan *et al.*, Plasmonic coupling at a metal/semiconductor interface. *Nat. Photonics* **11**, 806–812 (2017).
29. L. Collado *et al.*, Unravelling the effect of charge dynamics at the plasmonic metal/semiconductor interface for CO_2 photoreduction. *Nat. Commun.* **9**, 1–10 (2018).
30. N. Li *et al.*, Plasma-assisted photocatalysis of CH_4 and CO_2 into ethylene. *ACS Sustain. Chem. Eng.* **7**, 11455–11463 (2019).
31. L. Liu, A. Corma, Structural transformations of solid electrocatalysts and photocatalysts. *Nat. Rev. Chem.* **5**, 256–276 (2021).
32. L. Liu, A. Corma, Metal catalysts for heterogeneous catalysis: from single atoms to nanoclusters and nanoparticles. *Chem. Rev.* **118**, 4981–5079 (2018).
33. O. Ovsianytskyi *et al.*, Highly sensitive chemiresistive H_2S gas sensor based on graphene decorated with Ag nanoparticles and charged impurities. *Sensors Actuat. B: Chem.* **257**, 278–285 (2018).
34. X. Li *et al.*, In situ preparation of magnetic Ni-Au/graphene nanocomposites with electron-enhanced catalytic performance. *J. Alloy. Compd.* **706**, 377–386 (2017).
35. M. B. Boucher *et al.*, Single atom alloy surface analogs in $Pd_{0.18}Cu_{15}$ nanoparticles for selective hydrogenation reactions. *Phys. Chem. Chem. Phys.* **15**, 12187–12196 (2013).
36. X. Yu *et al.*, Plasmon-resonance-enhanced visible-light photocatalytic activity of Ag quantum dots/TiO_2 microspheres for methyl orange degradation. *Solid State Sci.* **80**, 1–5 (2018).
37. J. Huang *et al.*, Modification of Cu/SiO_2 Catalysts by La_2O_3 to quantitatively tune Cu^+-Cu^0 dual sites with improved catalytic activities and stabilities for dimethyl ether steam reforming. *ChemCatChem* **10**, 3862–3871 (2018).
38. F. Deng *et al.*, Evolution of active sites and catalytic consequences of mesoporous MCM-41 supported copper catalysts for the hydrogenation of ethylene carbonate. *Chem. Eng. J.* **334**, 1943–1953 (2018).
39. M. Liu *et al.*, High performance Au-Cu alloy for enhanced visible-light water splitting driven by coinage metals. *Chem. Commun.* **52**, 4694–4697 (2016).
40. W. S. Jiang *et al.*, Consciously constructing heterojunction or direct Z-scheme photocatalysts by regulating electron flow direction. *ACS Catal.* **8**, 2209–2217 (2018).
41. W. S. Jiang *et al.*, Deliberate construction of direct Z-scheme photocatalysts through photodeposition. *J. Mater. Chem. A* **7**, 18348–18356 (2019).
42. R. Jiang, B. Li, C. Fang, J. Wang, Metal/semiconductor hybrid nanostructures for plasmon-enhanced applications. *Adv. Mater.* **26**, 5274–5309 (2014).
43. J. Sheng *et al.*, Frustrated Lewis pair sites boosting CO_2 photoreduction on Cs_2CuBr_4 perovskite quantum dots. *ACS Catal.* **12**, 2915–2926 (2022).
44. N. Li, D. Geng, J. Zhou, Ag and Cu nanoparticles synergistically enhance photocatalytic CO_2 reduction activity of B phase TiO_2. *Catal. Lett.* **152**, 124–138 (2022).
45. N. L. Reddy *et al.*, Multifunctional Cu/Ag quantum dots on TiO_2 nanotubes as highly efficient photocatalysts for enhanced solar hydrogen evolution. *J. Catal.* **350**, 226–239 (2017).
46. S. Bhardwaj, B. Pal, Photodeposition of Ag and Cu binary co-catalyst onto TiO_2 for improved optical and photocatalytic degradation properties. *Adv. Powder Technol.* **29**, 2119–2128 (2017).
47. M. M. Momeni, P. Zeinali, Photochemical deposition of Ag, Cu, Cu@Ag, and Ag@Cu on TiO_2 nanotubes and their optical properties and photoelectrochemical activity. *J. Electron. Mater.* **50**, 5810–5818 (2021).
48. X. Ren *et al.*, Photocatalytic reduction of CO_2 on BiOX: Effect of halogen element type and surface oxygen vacancy mediated mechanism. *Appl. Catal. B Environ.* **274**, 119063 (2020).
49. Y. Wang *et al.*, Visible-light driven overall conversion of CO_2 and H_2O to CH_4 and O_2 on 3D-SiC@2D-MoS_2 heterostructure. *J. Am. Chem. Soc.* **140**, 14595–14598 (2018).

50. R. Zhang *et al.*, Photocatalytic oxidative dehydrogenation of ethane using CO_2 as a soft oxidant over Pd/TiO_2 catalysts to C_2H_4 and syngas. *ACS Catal.* **8**, 9280–9286 (2018).
51. N. Hayashi, H. Ishii, Y. Ouchi, K. Seki, Examination of band bending at buckminsterfullerene (C_{60})/metal interfaces by the Kelvin probe method. *J. Appl. Phys.* **92**, 3784–3793 (2002).
52. P. Sangpour, F. Hashemi, A. Z. Moshfegh, Photoenhanced degradation of methylene blue on cosputtered M: TiO_2 (M = Au, Ag, Cu) nanocomposite systems: A comparative study. *J. Phys. Chem. C* **114**, 13955–13961 (2010).
53. X. Yang *et al.*, Oxygen vacancies induced special CO_2 adsorption modes on Bi_2MoO_6 for highly selective conversion to CH_4. *Appl. Catal. B Environ.* **259**, 118088 (2019).
54. L. Liu, C. Zhao, J. T. Miller, Y. Li, Mechanistic study of CO_2 photoreduction with H_2O on Cu/TiO_2 nanocomposites by *in situ* X-ray absorption and infrared spectroscopies. *J. Phys. Chem. C* **121**, 490–499 (2016).
55. T. Di *et al.*, A direct Z-scheme g-C_3N_4/SnS_2 photocatalyst with superior visible-light CO_2 reduction performance. *J. Catal.* **352**, 532–541 (2017).
56. J. Y. Tang, R. T. Guo, W. G. Pan, W. G. Zhou, C. Y. Huang, Visible light activated photocatalytic behaviour of Eu (III) modified g-C_3N_4 for CO_2 reduction and H_2 evolution. *Appl. Surf. Sci.*, **467–468**, 206–212 (2019).
57. J. Wu *et al.*, Efficient visible-light-driven CO_2 reduction mediated by defect-engineered BiOBr atomic layers. *Angew. Chem. Int. Ed.* **57**, 8719–8723 (2018).
58. Z. Luan, J. A. Fournier, *In situ* FTIR spectroscopic investigation of active sites and adsorbate interactions in mesoporous aluminosilicate SBA-15 molecular sieves. *Micropor. Mesopor. Mat.* **79**, 235–240 (2005).
59. J. Wang *et al.*, A highly selective and stable ZnO-ZrO_2 solid solution catalyst for CO_2 hydrogenation to methanol. *Sci. Adv.* **3**, 1701290 (2017).
60. L. L. Cho, K. B. Huang, Identification of condom iubricants by FT-IR spectroscopy. *J. Forensic. Sci.* **11**, 33–40 (2012).
61. J. Murcia, M. C. Hidalgo, J. A. Navío, J. Araña, J. Doña-Rodríguez, *In situ* FT-IR study of the adsorption and photocatalytic oxidation of ethanol over sulfated and metallized TiO_2. *Appl. Catal. B Environ.* **142**, 205–213 (2013).
62. R. C. Brady, R. Pettit, Mechanism of the fischer-tropsch reaction. The chain propagation step. *J. Am. Chem. Soc.* **103**, 1287–1289 (1981).
63. S. Xie *et al.*, Photocatalytic and electrocatalytic transformations of C_1 molecules involving C-C coupling. *Energy Environ. Sci.* **14**, 37–89 (2020).
64. S. Ajmal *et al.*, Boosting C_2 products in electrochemical CO_2 reduction over highly dense copper nanoplates. *Catal. Sci. Technol* **10**, 4562–4570 (2020).
65. X. Nie, M. R. Esopi, M. J. Janik, A. Asthagiri, Selectivity of CO_2 reduction on copper electrodes: The role of the kinetics of elementary steps. *Angew. Chem.* **125**, 2519–2522 (2013).
66. X. Nie *et al.*, Mechanistic insight into C-C coupling over Fe-Cu bimetallic catalysts in CO_2 hydrogenation. *J. Phys. Chem. C* **121**, 13164–13174 (2017).
67. G. G. Kresse, J. J. Furthmüller, Efficient Iterative schemes for ab initio total-energy calculations using a plane-wave basis set. *Phys. Rev. B: Condens. Matter Mater. Phys.* **54**, 11169–11186 (1996).
68. J. Furthmüller, J. Hafner, G. Kresse, Dimer reconstruction and electronic surface states on clean and hydrogenated diamond (100) surfaces. *Phys. Rev. B: Condens. Matter Mater. Phys.* **53**, 7334–7351 (1996).
69. J. P. Perdew, K. Burke, M. Ernzerhof, Generalized gradient approximation made simple. *Phys. Rev. Lett.* **77**, 3865–3868 (1998).